agriculture

MDPI

Article

Early Detection of Muskmelon Powdery Mildew Using Time-Series 3D Multispectral Point Clouds

Zhiqi Hong [1,2,†], Qinghui Guo [1,3,†], Li Fang [4], Haiyan Cen [1,3] and Yong He [1,3,*]

[1] College of Biosystems Engineering and Food Science, Zhejiang University, Hangzhou 310058, China; hzq@zju.edu.cn (Z.H.); guoqinghui@tricaas.com (Q.G.); hycen@zju.edu.cn (H.C.)
[2] The Rural Development Academy & Agricultural Experiment Station, Zhejiang University, Hangzhou 310058, China
[3] Key Laboratory of Spectroscopy Sensing, Ministry of Agriculture and Rural Affairs, Hangzhou 310058, China
[4] Institute of Plant Protection and Microbiology, Zhejiang Academy of Agricultural Sciences, Hangzhou 310021, China; fangl@zaas.ac.cn
* Correspondence: yhe@zju.edu.cn
† These authors contributed equally to this work.

Abstract

Melon (*Cucumis melo* L.) is a globally significant horticultural crop, characterized by high nutritional value and substantial commercial status. However, frequent outbreaks of powdery mildew severely threaten its yield and fruit quality. Current early detection methods primarily focus on detached leaf assays, which often lack sufficient model generalization. This study proposes a temporal 3D multispectral point cloud reconstruction method for melon plants by integrating multispectral imaging with 3D reconstruction technology. An Artificial Neural Network (ANN) model for 3D spatial light field distribution was developed based on a hemispherical white reference to achieve precise reflectance calibration of the multispectral point clouds. Post-calibration, the coefficient of variation (*CV*) for the spectral reflectance of the hemispherical reference in 3D space was reduced to less than 2.4%. On this basis, an early classification model for melon powdery mildew was constructed using Partial Least Squares Discriminant Analysis (PLS-DA) based on the mean reflectance spectra of individual plant point clouds. The results demonstrate that the average recognition accuracy reaches 85.94% from 4 days post-inoculation onwards, enabling disease early warning three days in advance. This research provides critical theoretical support and technical reference for the non-destructive early monitoring and precision smart plant protection of crops in facility agriculture.

Keywords: muskmelon; powdery mildew; 3D multispectral point cloud; multispectral imaging; early detection; PLS-DA

Check for updates

Academic Editor: Thomas Thomidis

Received: 13 May 2026
Revised: 15 June 2026
Accepted: 23 June 2026
Published: 25 June 2026

Copyright: © 2026 by the authors. Licensee MDPI, Basel, Switzerland. This article is an open access article distributed under the terms and conditions of the Creative Commons Attribution (CC BY) license.

1. Introduction

Melon (*Cucumis melo* L.) is one of the most economically important crops in the Cucurbitaceae family. According to the Food and Agriculture Organization of the United Nations (FAO) statistical data in 2023, global melon production reached 28,467,920 tons, with a cultivation area of 1,068,238 hectares, and the industry scale continues to expand [1]. In 2022, China's melon production amounted to 13,868,000 tons, accounting for approximately 40% of the world's total output, making it the country with the largest cultivation area and the highest total yield. Powdery mildew is one of the most aggressive diseases in melon production, characterized by a short incubation period, strong epidemic potential,

year-round occurrence, and a high rate of secondary infection. It can afflict melon plants throughout the entire growth cycle, primarily infecting leaves, stems, and petioles, and under severe conditions, also affecting flowers and fruits. Infection of leaves produces white lesions, leading to premature senescence and reduced photosynthetic capacity, thereby severely compromising melon yield and fruit quality [2,3]. Present management practices are largely characterized by empirical assessments and a reactive 'spray-upon-symptom' approach, often precipitating the loss of the critical intervention window at the onset of infection. This results in excessive application of chemical pesticides and accelerates the development of pathogen resistance. Therefore, developing rapid, non-destructive, and accurate early detection technologies is critical for achieving effective disease management.

Spectral imaging technology, with its rapid, non-destructive, and precise characteristics, can acquire both image information of disease features and spectral reflectance values, enabling correlation analysis of disease characteristic information, making it an effective technical approach for addressing the challenge of early detection of powdery mildew [4]. In terms of modeling strategies based on spectral features, Bai et al. achieved effective identification of melon powdery mildew using full-band spectra combined with AdaBoost and Random Forest models [5]. Terentev et al., through a band selection strategy, used eleven key bands in combination with a support vector machine (SVM) algorithm to achieve very early detection of wheat leaf rust [6]. Zhang et al. further demonstrated that using vegetation indices as features can significantly improve the classification performance for tomato bacterial spot disease compared with raw spectra [7].

In terms of multi-feature fusion and model optimization, researchers have enhanced detection performance by integrating multi-source features—including spectral reflectance, textural characteristics, and vegetation indices—with more sophisticated modeling approaches. Zhao et al. combined visible–near-infrared (VIS/NIR) and near-infrared (NIR) spectral data and employed a principal component analysis-radial basis function (PCA-RBF) model to diagnose tomato leaf mold, achieving 100% accuracy on the calibration set and 99.3% on the prediction set [8]. Zhang et al. fused spectral features, vegetation indices, and textural features to construct a back-propagation neural network (BPNN) model for detecting and visualizing pear leaf anthracnose lesions, with the Optimal Wavelengths 2 (OWs2)-VIs-TFs-BPNN model attaining the highest classification accuracy of 98.61% [9]. Wu et al. utilized hyperspectral imaging combined with spectral features, vegetation indices, textural features, and an extreme learning machine (ELM) model, obtaining a classification accuracy of 96.67% for early detection of gray mold on strawberry leaves [10].

Deep learning networks, with their end-to-end representation learning capability, can automatically extract high-dimensional abstract features while simultaneously enabling visual localization of diseased regions. Ou et al. applied the competitive adaptive reweighted sampling (CARS) algorithm to select critical spectral features and vegetation indices, constructing a convolutional neural network (CNN) model with fused features that further improved the early identification accuracy of strawberry gray mold to 96.6% [11]. Liang et al. further utilized feature bands for image fusion and employed a Faster (Region-based Convolutional Neural Network) R-CNN model with a (Visual Geometry Group) VGG16 backbone for training, achieving a precise visual assessment of the spatial distribution of wheat Fusarium Head Blight (FHB) [12]. Nevertheless, the aforementioned studies predominantly employed detached leaves as experimental materials for indicator measurements. This approach not only suffers from destructive sampling, laborious procedures, and high labor costs but also relies heavily on controlled laboratory environments, rendering it incapable of achieving in situ and continuous early monitoring of crop diseases under field conditions.

To address the inherent limitations of in vitro assays, researchers have increasingly turned to on-plant detection performed at the original position. At the single-leaf level, Lay et al. employed hyperspectral imaging for the early detection of bacterial wildfire disease in potted soybean, achieving a classification accuracy exceeding 95% as early as 2–3 days post-inoculation by exploiting spectral differences in the near-infrared 700–710 nm band [13]. Castro-Valdecantos et al. combined hyperspectral imaging with machine learning to detect early physiological impairment caused by *Fusarium oxysporum* f. sp. *fragariae* in strawberry plants. They constructed artificial neural network (ANN) models based on spectral features from asymptomatic leaves, achieving 85% overall accuracy using stomatal conductance and 77% using photosynthetic rate, with a coefficient of determination (R^2) of 0.84 and 0.81, respectively [14]. Niu et al. utilized a LeafSpec device to acquire hyperspectral data from the second leaf of wheat and integrated spectral–temporal features with machine learning for the early detection of Septoria leaf blotch (SLB), reporting an overall Partial least squares discriminant analysis (PLS-DA) temporal classification accuracy of 96.97% based on mean spectra collected 3–17 days post-inoculation [15].

Although the aforementioned studies demonstrated promising in vivo detection performance using hyperspectral imaging, they were conducted exclusively at the single-leaf scale, capturing only localized characteristics of the plant and thus failing to represent the physiological status of the whole plant. This limitation restricts their practical applicability in field settings. To overcome the constraints of leaf-level detection, a growing body of research has sought to scale up from individual leaves to the whole-plant level. Hyperspectral imaging was employed to detect infections caused by *Fusarium commune* and *Rhizoctonia solani* in pakchoi plants, with a detection accuracy of 95.9% [16]. Hyperspectral imaging combined with deep learning was adopted by Bao et al. to detect *sugarcane smut* and *sugarcane mosaic* virus in sugarcane plants, and the detection accuracy was over 90% [17]. Powdery mildew on strawberry plants was predicted using the average reflectance spectra of plant canopies, and the prediction accuracy reached approximately 0.84 [18].

Despite these advances in whole-plant detection, challenges such as leaf occlusion and geometric pose interference persist. Three-dimensional point cloud technology, capable of capturing fine-scale structural information of plants that cannot be acquired through 2D imaging, has emerged as an efficient and non-invasive tool for plant phenotyping when integrated with artificial intelligence, and has thus garnered widespread attention and application [19–21]. Point clouds inherently provide depth information, enabling effective differentiation of overlapping leaves and stems, thereby overcoming the occlusion bottleneck inherent in 2D imaging. Nevertheless, plants are non-rigid living organisms whose morphology changes dynamically throughout growth. The processing of plant point cloud data continues to face numerous challenges that demand urgent resolution, most notably significant errors in multi-view registration and temporal alignment, as well as point cloud noise [22].

In the domain of three-dimensional multispectral plant detection, several research groups have successfully constructed 3D point cloud models. For instance, Liu et al. proposed a 3D point cloud registration approach to replace conventional 2D multispectral image registration, accomplishing five-band (UV, blue, green, red, and near-infrared) point cloud alignment directly in three-dimensional space, thereby overcoming the limitations of 2D registration in non-planar and structurally complex scenes [23]. Roscher et al. integrated hyperspectral imaging with 3D point cloud reconstruction to build hyperspectral 3D plant models, which improved the detection accuracy of Cercospora leaf spot disease symptoms on sugar beet plants [24]. Xiao et al. employed multi-view spectral images combined with the Structure from Motion (SfM) algorithm, using only a single multispectral sensor to construct a 3D CLS (Cercospora leaf spot) point cloud model. The approach achieved a

disease severity classification accuracy of 75%, and the estimated disease incidence exhibited strong agreement with ground-truth measurements, yielding a root mean square error (RMSE) of 8.4% [25]. Yang et al. performed multi-view close-range imaging of flowering Chinese cabbage and kale plants, integrating U^2-Net with an improved SfM pipeline to achieve high-fidelity three-dimensional plant phenotyping reconstruction, with both plant height and width prediction achieving R^2 values exceeding 0.99 [26]. Notably, the aforementioned studies have predominantly focused on the construction of 3D multispectral point clouds, while their application to the detection of actual crop physicochemical properties remains limited. A key bottleneck is that 3D multispectral point cloud data require rigorous calibration before they can reliably reflect crop disease status.

In complex plant canopy environments, mutual occlusion among leaves, edge curling, and non-planar structures lead to incomplete spectral information acquisition based on two-dimensional imaging. Moreover, the three-dimensional geometric posture of leaves significantly interferes with the reflected spectral signal, rendering conventional calibration methods based on a planar white reference invalid and severely compromising diagnostic accuracy. Zhang et al. proposed a 3D white reference method based on the fusion of hyperspectral images and 3D point clouds, effectively correcting reflectance and Normalized Difference Vegetation Index (NDVI) errors in soybean leaves caused by angular variations [27]. Zhang et al. further developed an improved image calibration model, SVR, integrating leaf hyperspectral images and 3D point clouds to eliminate the interference of leaf angle on reflectance spectra and NDVI, with the corrected results approaching the standard of horizontal leaves [28]. However, these methods are only applicable to unobstructed indoor leaves, have limited generality, and do not achieve full-spectrum calibration. Xie Pengyao et al. proposed a novel method for generating high-quality plant three-dimensional multispectral point clouds by fusing a snapshot spectral camera and an RGB and depth camera, combined with an improved Speeded Up Robust Features-Demons (SURF-Demons) registration algorithm and hemispherical reference body correction, significantly enhancing the spectral accuracy of 3D multispectral point clouds [29]. The reflectance correction method based on the hemispherical reference combined with an artificial neural network (ANN) achieved a coefficient of determination (R^2) of 0.962 and an RMSE of 0.036. Compared with the ground truth measured by an Analytical Spectral Devices (ASD) spectrometer, the average RMSE of reflectance spectra at different leaf positions after correction was reduced by 78.0%, and the average Euclidean distance between multi-view reflectance spectra at the same leaf position was reduced by 60.7%. However, this method requires a dual-camera system (RGB-D and multispectral), which entails higher costs and increases data processing time and errors during the image registration step, thereby limiting its applicability in large-scale field deployment.

Given the limitations of existing detection technologies in terms of missing spatial structural information, weak generalization capability, and high costs, this study proposes a 3D multispectral online detection method for melon powdery mildew based on a low-cost single-camera system. By extracting 3D spatial features from hemispherical white references and integrating an Artificial Neural Network (ANN), we constructed a spatial light field distribution model. This approach is designed to mitigate system errors caused by non-uniform wavelength distribution, sensor spectral response discrepancies, and environmental scattering, enabling accurate illumination prediction and reflectance correction for leaves regardless of their pose. By collecting time-series in vivo data from melon plants, a Partial Least Squares Discriminant Analysis (PLS-DA) model for melon powdery mildew was constructed, offering a novel technical approach for low-cost, high-accuracy early warning of crop diseases in protected agricultural environments.

2. Materials and Methods

2.1. Data Acquisition

In this study, the muskmelon cultivar "Zhetian 501" was used as the research object. Seeds were soaked in deionized water for 3 h and then placed in an artificial climate chamber at 28–30 °C for 48 h to promote germination. Once the radicles emerged, the seeds were transferred to nursery pots and cultivated in an environment with 90% relative humidity. After emergence, seedlings were transplanted to a research greenhouse with environmental settings of 28 °C during the day, 18 °C at night, and 80% relative humidity. When the seedlings reached the "three-leaf and one-heart" stage, 30 plants with uniform growth were selected for the pathogen inoculation experiment. The experiment consisted of an inoculation group (20 plants) and a control group (10 non-inoculated plants). Inoculation with powdery mildew spores was performed on the evening of 14 July 2025. Following inoculation, the plants remained in the greenhouse overnight to facilitate spore germination. From 15 July to 25 July 2025, 3D multispectral images and multi-view RGB images of the muskmelon seedlings were periodically collected. During the experimental period, the greenhouse environment was strictly managed via an environmental control system, maintaining temperatures of 25 °C during the day and 20 °C at night, with nighttime relative humidity controlled at approximately 85%. Standardized water and fertilizer management was implemented to ensure normal plant growth and stable disease development.

A self-developed plant 3D phenotyping platform was utilized to acquire multi-view RGB and multispectral images of the muskmelon plants in this experiment. The platform integrates a conveyor mechanism, a multi-view RGB 3D imaging module, and a multispectral 3D reconstruction module. The RGB imaging module was equipped with five circumferentially distributed industrial cameras (iRAYPLE, A3B00CG000). Triggered by a rotation mechanism at 20° intervals, a total of 90 images were acquired for each plant. The multispectral reconstruction module consisted of a top-mounted tungsten-halogen light source (60 W) and a side-mounted multispectral camera (MQ022MG-CM, XIMEA, Münster, Germany). Driven by the rotating platform, one image was captured every 10°, resulting in 36 multispectral images per plant. Each multispectral image contained 25 spectral bands, covering a range of 650–950 nm. Prior to data acquisition, camera dark current correction was performed by capturing dark reference images with the light source turned off. All subsequent calculations were conducted using the net values after subtracting the dark background. For each plant, 90 RGB images and 36 multispectral images were collected for each muskmelon plant every day. All images were imported into Metashape 2.1.0 to separately reconstruct RGB and multispectral 3D point clouds for each muskmelon seedling. The complete workflow for generating plant multispectral 3D point clouds is described in Section 2.3. Paired RGB-multispectral 3D point cloud data of 20 infected plants and 10 healthy plants were acquired daily throughout the experiment. The entire data acquisition experiment lasted for 11 consecutive days. In total, 220 groups of time-series 3D point clouds (220 RGB point clouds and 220 multispectral point clouds) were obtained for inoculated plants, while 110 groups of time-series 3D point clouds (110 RGB point clouds and 110 multispectral point clouds) were collected for healthy plants. Subsequently, the average spectra of all time-series multispectral 3D point clouds from 110 healthy muskmelon plants and 220 powdery mildew-inoculated muskmelon plants were calculated, yielding 330 average spectral profiles in total (110 spectra from healthy plants and 220 spectra from inoculated plants). All 330 average spectra were divided into a training set and a validation set at a ratio of 3:1 to establish a Partial Least Squares Discriminant Analysis (PLS-DA) discriminant model for powdery mildew detection on muskmelon plants. Detailed procedures for model construction and evaluation metrics are presented in Sections 2.4 and 2.5, respectively.

Five solid Teflon hemispheres with a diameter of 100 mm, machined using computer numerical control (CNC) and surface-treated to be matte, were used as references. Five vertical positions (0, 10 cm, 20 cm, 30 cm, 40 cm) were selected at equal intervals within the plant height range to develop a spatial distribution model of light intensity under a point light source. At each position, five hemispherical references were randomly placed five times for multispectral data acquisition (Figure 1a), resulting in a total of 25 sets of calibration data. To compensate for the lack of surface texture on the hemisphere, which typically hinders 3D reconstruction, black markers with a diameter of 3 mm were randomly attached to the hemispherical surface (Figure 2a).

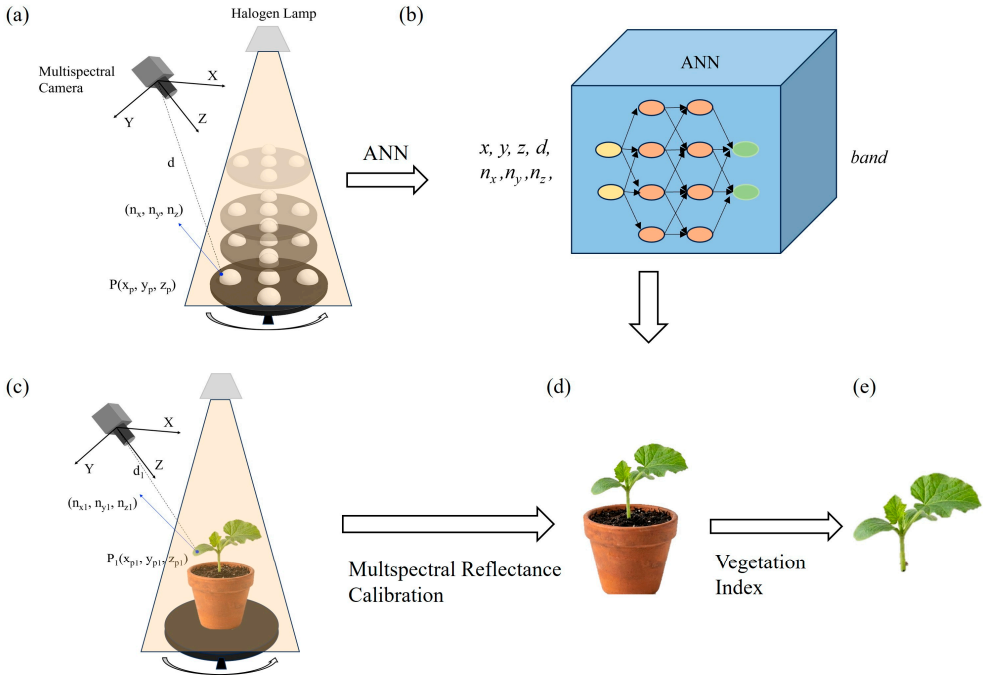

Figure 1. (**a**) Acquisition of multispectral images of the hemispherical white references at different heights; (**b**) Architecture of the ANN model for 3D spatial light field distribution; (**c**) Multispectral image acquisition of muskmelon plants; (**d**) 3D multispectral point clouds of muskmelon plants; (**e**) Background removal of muskmelon 3D multispectral point clouds based on vegetation indices.

2.2. Generation of 3D Multispectral Point Clouds

The original multispectral images, with a resolution of 2048 × 1088, were parsed using pixel units (5 × 5) into a multispectral data cube of 409 × 217 × 25. Due to the reduction in resolution after parsing, which results in sparse feature points, the original multispectral images were directly used to construct the 3D point cloud of the hemispherical white reference based on the SfM-MVS algorithm in this study. Following point cloud generation, precise mapping of multispectral information and background removal were achieved through the following steps:

(1) Projective Matching: Any point P within the 3D point cloud was projected onto each original image to obtain the corresponding projection point P_n through the utilization of the camera's intrinsic and extrinsic parameter matrices (Formula (1)). The angle between the normal vector n and the line connecting point P to the projection point P_n was calculated, after which the effective projection perspectives with angles smaller than 15°, 20°, 25°, and 30° were respectively retained (Figure 2a).

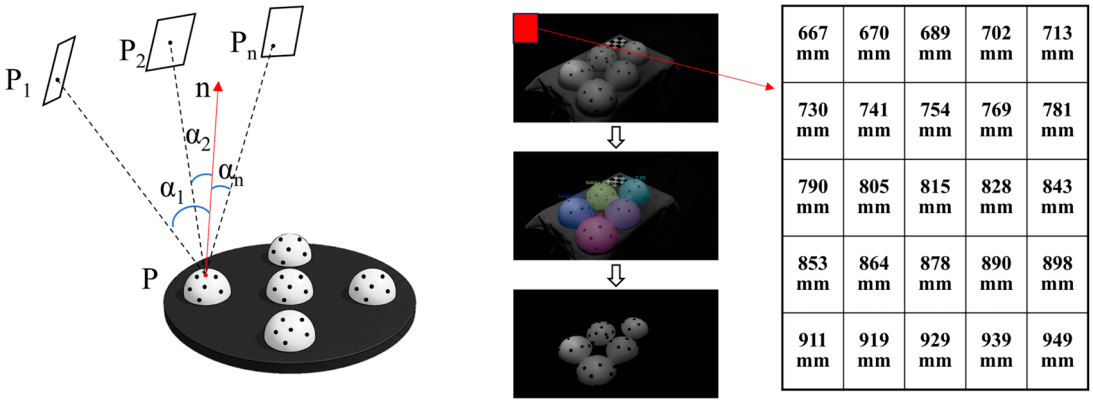

Figure 2. (**a**) Mapping Relationship between 3D Point Cloud and Multispectral Images of the Hemispherical White Reference; (**b**) Background Removal and Spectral Extraction of the Hemispherical White Reference Multispectral Images. Note: P denotes an arbitrary point within the 3D multispectral point cloud, and P_1, P_2, $\cdots$, P_n represent the projection points of P onto different multispectral images, respectively. The angles formed between P and each corresponding projection point are defined as α_1, α_2, $\cdots$, α_n and so forth.

(2) Target Extraction: A set of raw multispectral image data of the hemispherical white reference was arbitrarily selected from five different height positions. A total of 180 images (36 images per set) were utilized for the annotation of the hemispherical white reference. The annotated data were randomly partitioned into a training set and a validation set according to a 3:1 ratio for the training of a YOLOv8 model.

The training parameter settings for this model are as follows: the number of iterations (epochs) was set to 100, and the batch size was set to 32 to ensure the stability of gradient descent. The input image size was uniformly adjusted to 640 × 640 pixels. The model employed the AdamW optimizer for weight updates, with the initial learning rate set at 0.01. These configurations were designed to balance the convergence speed and detection accuracy of the model, thereby providing reliable support for the subsequent automated extraction of hemispherical white reference targets. Subsequent to the model training, the hemispherical white references within the multispectral images were identified, and the black markers on the white spheres were removed based on color thresholds. Consequently, purified multispectral images of the hemispherical white reference were obtained (Figure 2b).

(3) Spectral Mapping: Whether the effective projection points were situated within the hemispherical regions identified by YOLOv8 was determined, and the mean pixel values of a 5 × 5 window corresponding to these points were extracted as the band values. If any pixel within the window was located outside the identified region, the projection was judged to be invalid. Ultimately, the average of the mapping values from all effective views was taken as the spectral information for each respective point.

$$s[u;\ v;\ 1] = K \cdot [R \mid t] \cdot [X_w;\ Y_w;\ Z_w;\ 1] \quad (1)$$

In the formula, u and v represent the pixel coordinates of a 3D point on the 2D image respectively; s is the scale factor, which equals the depth value from the point to the optical center of the camera; K denotes the camera intrinsic matrix; $[R \mid t]$ is the camera extrinsic matrix, representing the rotation and translation of the camera in the world coordinate system; and Xw, Yw and Zw respectively denote the spatial coordinates of any point in the point cloud under the world coordinate system.

(4) Vegetation Reconstruction: A similar approach was adopted for the construction of the 3D multispectral point clouds of the muskmelon plants. Subsequent to the construction, background noise was removed based on the normalized difference vegetation index (*NDVI*) (Formula (2)) [30]. Vegetation spectra typically exhibit a sharp rise in reflectance within the red-edge region of 700–740 nm. Two characteristic wavebands, namely 702 nm in the red-edge range and 741 nm at the boundary between the red-edge and near-infrared regions, were selected in this study to construct spectral indices. These indices were used to amplify the spectral differences between plants and background features, thereby achieving effective separation of plant targets from background noise. Finally, scale calibration for all point clouds was performed through the utilization of the known dimensions of the flower pots.

$$NDVI = \frac{NIR - Red}{NIR + Red} \tag{2}$$

In the formula, *NDVI* stands for normalized difference vegetation index; *NIR* denotes the reflectance in the near-infrared band; *Red* denotes reflectance in the red band.

Subsequent to the acquisition of the multi-view RGB images of the muskmelon plants, 3D point cloud data of the muskmelon were constructed via the SfM-MVS method. Background noise within the point clouds was eliminated through the application of color thresholds, by which the true status of the plants was enabled to be displayed.

2.3. Reflectance Calibration of 3D Multispectral Point Clouds

To eliminate the spatial light field differences caused by non-uniform illumination from point light sources, the following steps were adopted for reflectance calibration: Firstly, the coordinate system was unified, wherein the optical center of the multispectral camera was set as the origin, the optical axis was designated as the *Z*-axis, and the imaging plane was defined as the xoy plane. From the 3D multispectral point clouds of the hemispherical white reference at various heights, the spatial coordinates (x, y, z), normal vectors (n_x, n_y, n_z), distance to the origin d, and digital number (DN) values of the 25 bands were extracted.

Secondly, a 3:1 ratio was applied to partition the calibration data into a correction set and a validation set, following which a 3D spatial light field distribution model based on an Artificial Neural Network (ANN) was constructed (Figure 1b). For each of the 25 spectral bands of the hemispherical white reference, independent modeling was performed. The architecture of the ANN model was mainly composed of an input layer (comprising x, y, z, n_x, n_y, n_z, d), five hidden layers, and one output layer. A dropout layer was included after each hidden layer to reduce overfitting. Furthermore, the ReLU function was utilized as the activation function, Adam was selected as the optimizer, and Mean Squared Error (MSE) was adopted as the loss function.

After the model was constructed, the same coordinate transformation was applied to the 3D point cloud of the muskmelon plant. For any given point, the 3D spatial features (x, y, z, n_x, n_y, n_z, d) were extracted and subsequently input into the constructed model to achieve the prediction of the hemispherical white reference light intensity at that specific location. Finally, the calculation and calibration of the multispectral reflectance for any point on the muskmelon were implemented by the utilization of Formula (3).

$$R = \frac{D_{plant}}{D_{ref}} \times 100\% \tag{3}$$

2.4. Model Construction

After the calibration of the 3D multispectral reflectance point clouds of the muskmelon plants was completed, the reflectance spectra of all points for each plant were averaged. A total of 30 melon plants were measured continuously for 11 days, including 20 inoculated plants and 10 blank control plants. In total, 220 average spectral data were obtained from the inoculated group (20 plants × 11 days) and 110 average spectral data from the control group (10 plants × 11 days), yielding a total of 330 spectral samples. Based on the daily muskmelon spectral data, a 3:1 ratio was applied to randomly partition the data into a training set and a validation set. We constructed one unified Partial Least Squares Discriminant Analysis (PLS-DA) model using all collected observations to realize time-series identification of muskmelon powdery mildew. Partial least squares discriminant analysis (PLS-DA) is a linear classification algorithm derived from partial least squares regression (PLSR). This algorithm simultaneously decomposes the independent variable matrix X (spectral data) and the dummy response matrix Y (binary labels for healthy and infected samples) to extract latent variables that maximize the covariance between X and Y. In this dataset, healthy muskmelon samples were assigned a label of 0, while infected samples were assigned a label of 1. Samples with predicted Y values greater than 0.5 were classified as infected, and those with predicted Y values less than 0.5 were classified as healthy. Notably, spectral measurements of 30 muskmelon plants (10 healthy and 20 infected) were collected over 11 consecutive days in this study. Instead of constructing a separate PLS-DA model for every single day, only one unified PLS-DA discriminant model was established. The established PLS-DA model was used to classify samples collected on all days. The average recognition accuracy of muskmelon powdery mildew from the n-th day post-inoculation onwards was adopted to evaluate model performance, as detailed in Equation (8).

2.5. Model Evaluation

The development of the algorithms and the calculation of metrics involved in this research were completed within the environments of Python 3.9 (integrated with PyTorch and Scikit-learn libraries) and MATLAB 2021b, respectively.

To comprehensively evaluate the performance of the relevant algorithms, five groups of multispectral images of the hemispherical white reference were randomly selected and manually annotated, whereby the pixel regions of the hemispherical white reference were distinguished from background noise. Furthermore, the accuracy of the hemispherical white reference identification was assessed through the utilization of *Precision* (Formula (4)) and *Recall* (Formula (5)).

$$P = \frac{TP}{TP + FP} \times 100\% \tag{4}$$

$$R = \frac{TP}{TP + FN} \times 100\% \tag{5}$$

In the formula, TP denotes the number of correctly identified hemispherical white reference pixels in the multispectral image; FN denotes the number of misclassified hemispherical white reference pixels in the multispectral image; FP denotes the number of misclassified non-hemispherical white reference pixels in the multispectral image; P represents the precision of hemispherical white reference region recognition; and R represents the recall of hemispherical white reference region recognition.

The coefficient of determination R^2 (Formula (6)) and the Root Mean Square Error (*RMSE*) (Formula (7)) were adopted to evaluate the 3D spatial light field distribution model based on ANN. The ability of the model to capture the non-linear mapping relationship

between the spatial geometric features and the DN values of the hemispherical white reference spectra is reflected by R^2. A value closer to 1 indicates that a higher degree of explanation for the light field distribution on the surface of the white sphere is provided by the model. Meanwhile, the physical extent to which the predicted band values deviate from the true spectral values is directly reflected by the *RMSE*, where a smaller numerical value represents that more accurate spectral information was reconstructed by the model.

$$R^2 = 1 - \sum_{i=1}^{n} \frac{(y_i - \hat{y}_i)^2}{(y_i - \overline{y}_i)^2} \tag{6}$$

$$RMSE = \sqrt{\frac{1}{n} \sum_{i=1}^{n} (y_i - \hat{y}_i)^2} \tag{7}$$

In the formula, y_i is the measured spectral DN value of the i-th sampling point in the white sphere point cloud; $\hat{y}_i$ is the predicted value of the ANN model; y_i is the mean of the measured values of all samples; and n denotes the number of point cloud samples in the test set.

To investigate the performance of the model under different infection time series, particularly the discriminant ability for the early stages of muskmelon powdery mildew infection, the classification accuracy (ACC_{day}) was adopted in this research for the evaluation of PLS-DA and related discriminant models (Formula (8)).

$$ACC_{dayn} = \frac{N_c}{N_t} \times 100\% \tag{8}$$

In the formula, ACC_{dayn} denotes the average recognition accuracy of muskmelon powdery mildew from the n-th day post-inoculation onwards; N_c is the number of muskmelon plants correctly classified as diseased or healthy; and N_t is the total number of samples. The uniformity of the DN values of the hemispherical white reference before calibration and the reflectance after calibration was evaluated through the utilization of the coefficient of variation (Formula (9)).

$$CV = \frac{\sigma}{\mu} \tag{9}$$

In the formula, CV represents the coefficient of variation of DN values (or reflectance) for the 3D point cloud calibrated by the hemispherical white reference; σ and μ denote the standard deviation and mean value of DN values (or reflectance) for the 3D point cloud calibrated by the hemispherical white reference, respectively.

3. Results

3.1. Target Recognition and Mask Extraction of the Hemispherical White Reference

Through the YOLOv8 model, the hemispherical white references placed at different height positions were accurately identified, as illustrated in Figure 3. Identification precision and recall of the white sphere regions were recorded as 97% and 99%, respectively. In Figure 3a, symmetric rectangular protrusions were observed on the sphere masks near the tangent points. This phenomenon was primarily caused by the spatial induction from the regression components of the bounding boxes during mask synthesis by the YOLOv8 segmentation algorithm. At the tangent points, because the tangents of the circular arcs are parallel to the boundaries of the bounding boxes, the local spatial feature responses of the model coincide with the rectangular boundaries, whereby an overflow of the mask prototypes toward the corners occurred during the assembly process [31].

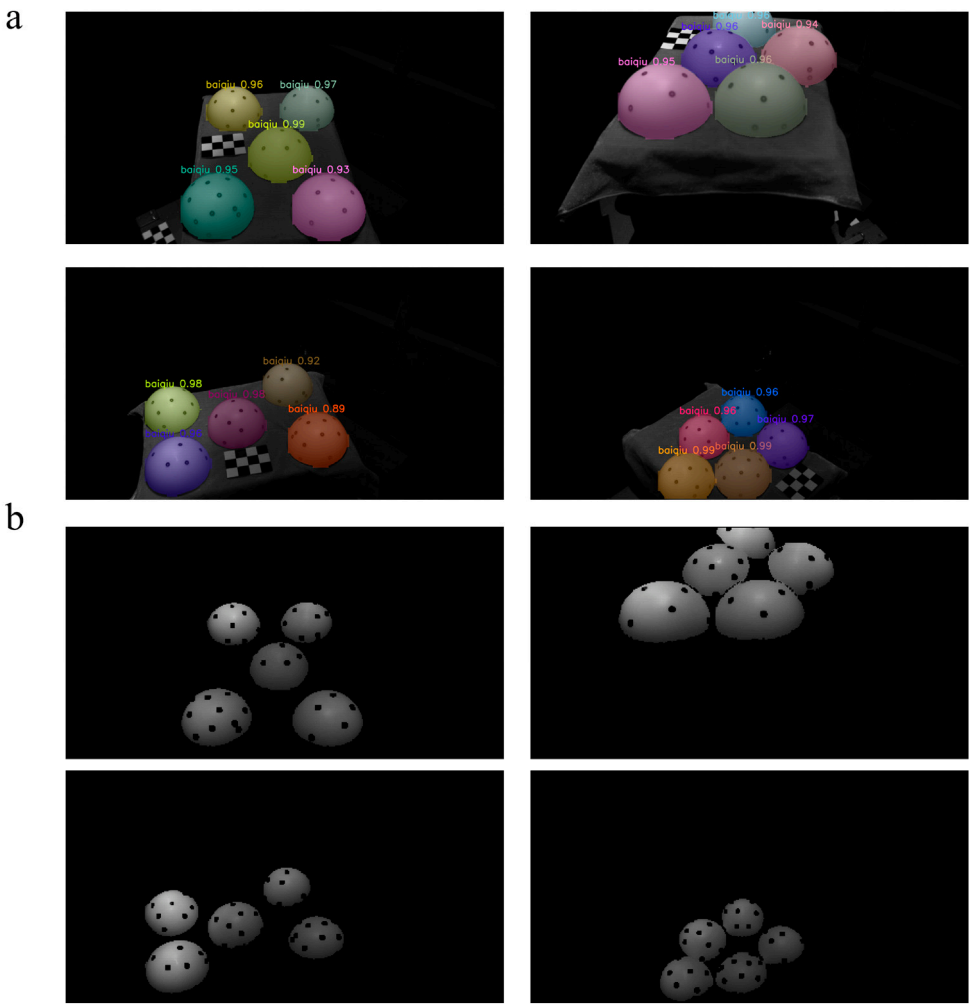

Figure 3. (**a**) Target detection results of the hemispherical white reference in multispectral images; (**b**) Background removal results of the hemispherical white reference in multispectral images.

As shown in Figure 3b, through the implementation of low-threshold removal of spectral DN values and morphological erosion of the edges on the identified hemispherical reference mask regions, the precise extraction of white sphere targets and the effective stripping of black markers on their surfaces were successfully achieved in this research. Although some sampling pixels at the edges and marker locations were proactively discarded by this method, the penumbra effect caused by the sphere curvature and the leakage of background pixels were circumvented via edge erosion, provided that the overlap required for the reconstruction of the 3D multispectral point clouds of the hemispherical white reference was guaranteed. Furthermore, by utilizing thorough denoising at the image level, the automated and high-precision stripping of point cloud background noise in 3D space was realized, by which purified data were provided for the subsequent construction of the 3D spatial light field distribution model.

3.2. Impact of Projection Constraint Angle on the Accuracy of the Spatial Light Field Distribution Model

The threshold for the angle between the projection vector and the point cloud normal vector was identified as a key factor affecting the quality of 3D multispectral reconstruction and the accuracy of the light field distribution model. As presented in Table 1, a trend of initially increasing and subsequently decreasing performance was exhibited by the spatial light field distribution model as the angle threshold was varied. When the angle threshold was set to 20°, the optimal fitting effect was demonstrated by the model, wherein the

coefficients of determination (R^2) for the training and validation sets reached 0.885 and 0.872, respectively, while the Root Mean Square Errors (*RMSE*) were recorded as 5.717 and 6.313.

Table 1. Impact of different projection constraint angles on the accuracy of the light field distribution models.

Angle	R^2_c	$RMSE_c$	R^2_p	$RMSE_p$
15°	0.823	12.436	0.818	13.014
20°	0.885	5.717	0.872	6.313
25°	0.859	8.301	0.838	8.851
30°	0.805	14.011	0.795	14.325

This phenomenon occurred primarily because, when the angle constraint was excessively small, the number of effective projection points satisfying the constraint conditions was significantly reduced, although the selected pixels were closer to the quasi-specular reflection in the normal direction, consistent with the physical assumption of near-vertical observation. Not only was a relatively sparse spatial distribution of the 3D point cloud caused by this limitation, but it also became difficult for the ANN model to capture the continuous variation patterns of the complex light field in 3D space due to the non-uniform distribution of samples within the training set.

Conversely, when the angle threshold was set too large, the spectral attributes of a single point cloud were fused from a greater number of image projections obtained under large-angle observations. According to the Bidirectional Reflectance Distribution Function (BRDF) theory, significant anisotropic changes are exhibited by the reflection characteristics of the target surface as the observation angle increases. By the introduction of such large-angle projection data, not only was more radiation noise injected due to observational geometric distortion, but geometric errors were also introduced because of spatial registration deviations during the multi-view fusion process, whereby the ability of the model to capture the continuous distribution patterns of the light field was weakened [32]. Therefore, an appropriate projection constraint angle must be established to balance the spatial sampling integrity of the point cloud with the precision of the radiation data.

3.3. Correction Results of the 3D Point Cloud Reflectance for the Hemispherical White Reference

The radiance (DN) of the original hemispherical white reference at the 730 nm band exhibited significant spatial heterogeneity, whereby a "gradient distribution" pattern, attenuating from the central axis of the sphere toward the edges, was presented, as illustrated in Figure 4a. It was demonstrated by the experimental data that the sampling height exerts a decisive influence on the uniformity of the radiation distribution; within the height range of 10 cm to 40 cm, the coefficients of variation (*CV*) of the point clouds were recorded as 27.9%, 32.2%, 36.6%, and 45.5%, respectively. As the height of the hemispherical white reference increased, the DN values on the hemispherical surface gradually increased, and the non-uniformity of the distribution was intensified, indicating the non-uniform radiation characteristics of the point light source within the 3D space of the phenotyping platform. The closer the hemisphere was to the light source, the steeper the radial gradient of the energy distribution on the white sphere became. Furthermore, acute fluctuations in the radiation response were caused by subtle changes in the angle between the surface normal vector of the sphere and the incident light rays, whereby severe spectral artifacts were generated for the same homogeneous target at different spatial locations.

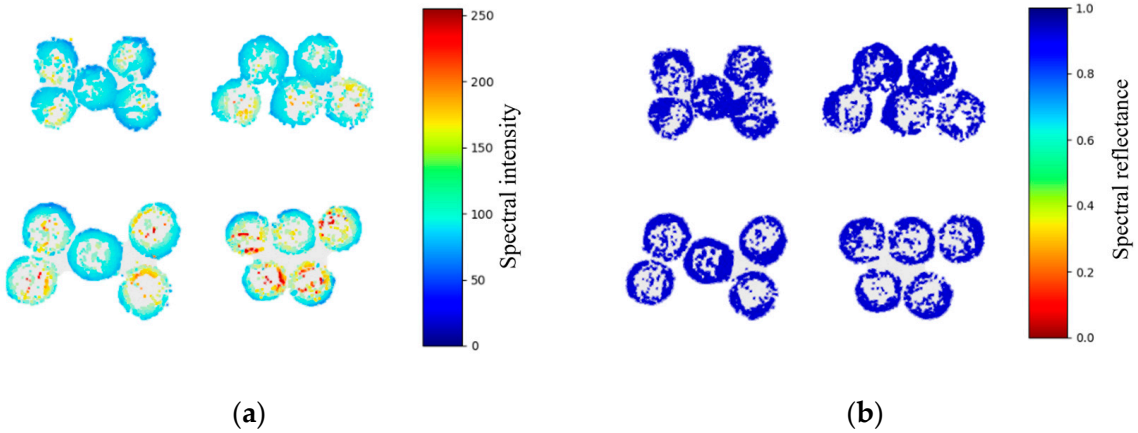

Figure 4. (**a**) Spatial distribution of 730 nm DN values of the hemispherical white reference 3D point cloud before calibration; (**b**) Spatial distribution of 730 nm relative reflectance of the hemispherical white reference 3D point cloud after calibration.

After the correction was performed by applying the spatial light field distribution model constructed in this research (Figure 4b), a high degree of spatial consistency was achieved for the relative reflectance of the white sphere 3D point clouds at 730 nm. The corrected reflectance values were consistently stabilized above 95%, and the coefficients of variation across different heights were all found to be less than 2.4%, whereby the accurate transformation from environment-dependent "radiance" to the inherent "reflectance" of the object was realized. Through deep learning, the radiation gain deviations caused by distance attenuation and surface geometric orientation were effectively compensated for by the model. It was demonstrated by the experiments that the model possesses extremely strong spatial generalization capability and reconstruction robustness, by which high signal-to-noise ratio fundamental data can be provided for the subsequent reflectance calibration of 3D multispectral point clouds of plants.

3.4. Application of Temporal 3D Reflectance Spectra in the Early Identification of Muskmelon Powdery Mildew

In this study, spectral data from three bands (702 nm, 741 nm, and 828 nm) were selected to synthesize temporal 3D multispectral pseudo-color point clouds by mapping them to the RGB channels (Figure 5a). A comparative analysis with conventional temporal RGB 3D point clouds (Figure 5b) revealed that the multispectral 3D point clouds possess a robust capacity for plant structure restoration. They are capable of completely reproducing the morphological structure and spatial characteristics of muskmelon leaves, thereby providing comprehensive data support for leaf disease identification and feature extraction. However, due to the inherent spatial structure of the plants, leaves tend to occlude the stems. Multispectral images captured from a single perspective cannot acquire spectral information from the stem regions, resulting in a lack of stem points within the multispectral point clouds. Considering the pathogenic characteristics of muskmelon powdery mildew, the disease primarily infects leaf tissues, while stems rarely exhibit symptoms. Consequently, the missing stem point cloud data does not interfere with the identification and detection results of the powdery mildew, ensuring high overall data validity.

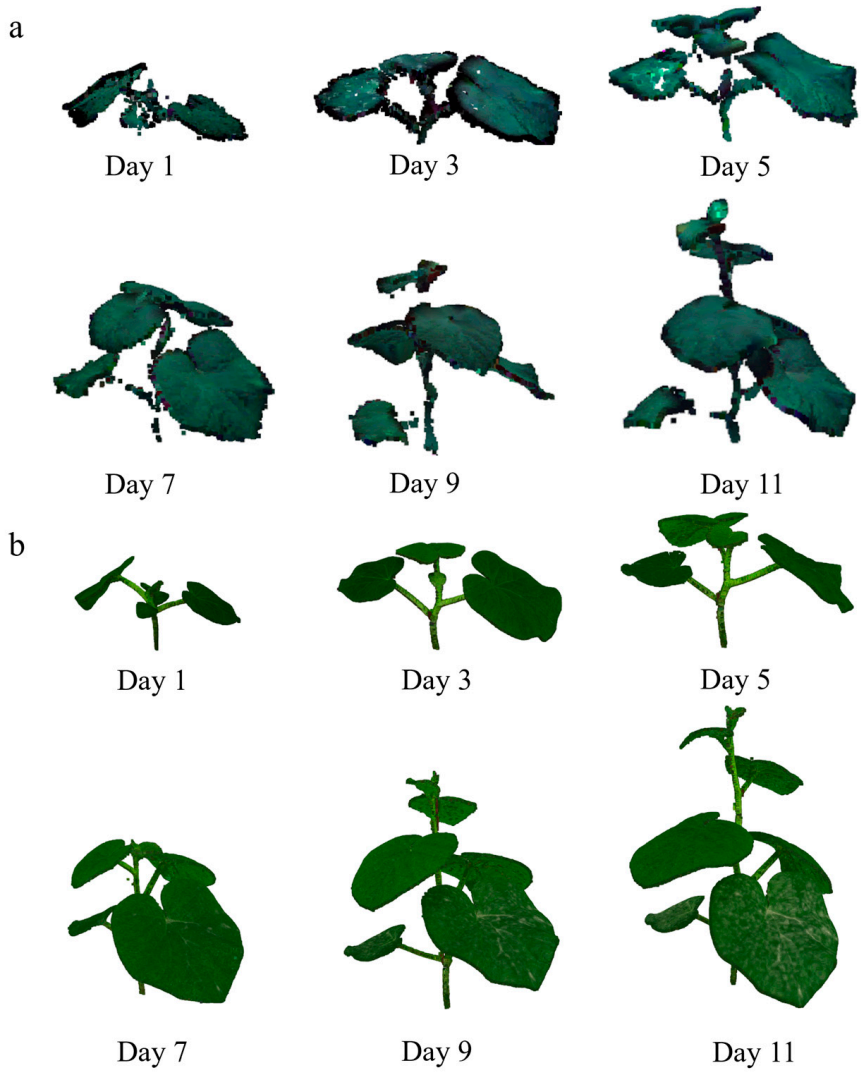

Figure 5. (**a**) Temporal 3D multispectral pseudo-color point clouds of muskmelon; (**b**) Temporal RGB 3D point clouds of muskmelon.

The complete pathogenic progression of muskmelon powdery mildew can be clearly observed through the temporal RGB 3D point clouds. Seven days after the plants were inoculated with the pathogen, sporadic white lesions began to appear on the leaves, indicating a mild state of infection (Figure 5b). As the cultivation time progressed, the disease continued to infect and spread. By the 11th day post-inoculation, the coverage area of the lesions on the muskmelon leaves had significantly increased, with symptoms appearing clear and typical. This sequence fully presents the dynamic pathogenic process of muskmelon powdery mildew, ranging from the incubation period to the manifestation of symptoms.

The temporal variations in average spectra of melon plants after inoculation are shown in Figure 6. Spectral curves at different time points exhibited similar trends, with a distinct increase in reflectance within the 670 nm–740 nm range, which corresponds to the typical vegetation red-edge effect. The average spectral reflectance of melon plants increased gradually as powdery mildew infection became more severe. This is because the pathogen induces a reduction in leaf chlorophyll content, which weakens the absorption of visible light and consequently leads to a continuous rise in overall reflectance [5].

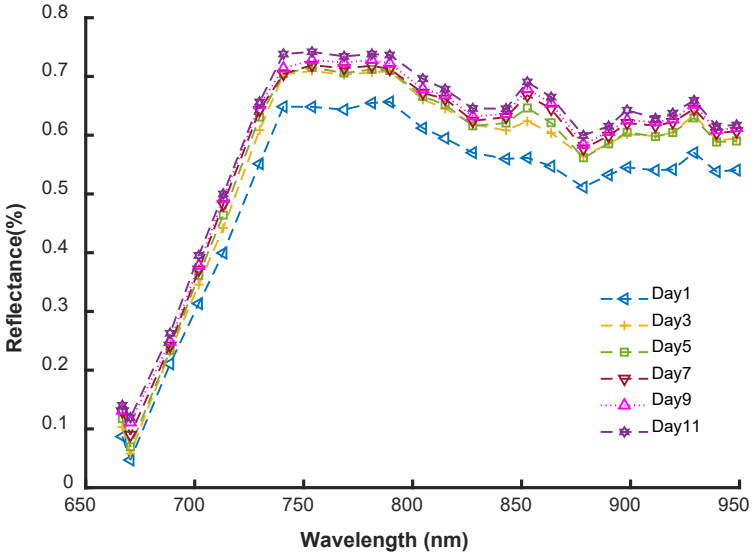

Figure 6. Time-series spectral variations of melon plants after inoculation.

To achieve the accurate identification and early prediction of muskmelon powdery mildew, the mean reflectance spectra of individual plant point clouds were extracted in this study to construct a Partial Least Squares Discriminant Analysis (PLS-DA) model. Table 2 shows the recognition results of muskmelon powdery on different sampling days. It can be observed from the table that the model achieved poor recognition performance for melon plants on the first day after powdery mildew inoculation, with an accuracy of only 54.04%. As the severity of melon powdery mildew infection gradually increased, the daily discrimination accuracy of the model for identifying infected melon plants rose continuously, increasing from the initial 54.04% to a maximum value of 93.48%. The overall temporal modeling results revealed an average discriminant accuracy of 83.49% for the training set and 76.79% for the validation set, with an overall average accuracy of 80.79%, which demonstrates the stable and reliable discriminant capability of the model for muskmelon powdery mildew.

Table 2. Discriminant results of muskmelon powdery mildew across different time series.

Day	Training Set Accuracy (%)	Validation Set Accuracy (%)	Average Accuracy (%)
1	65.22%	42.86%	54.04%
2	73.91%	57.14%	72.67%
3	86.36%	62.50%	74.43%
4	81.82%	75.00%	78.41%
5	86.36%	75.00%	80.68%
6	82.61%	87.50%	85.06%
7	86.36%	85.71%	86.04%
8	86.96%	85.71%	86.34%
9	95.45%	85.71%	90.58%
10	86.96%	100.00%	93.48%
11	86.36%	87.50%	86.93%
Average accuracy (%)	83.49%	76.79%	80.79%

Since single-day detection results are prone to random fluctuations induced by environmental factors and plant physiological variations, we further introduced the cumulative average classification accuracy ACC_{dayn}, which covers data from Day n to the last sampling day, to comprehensively evaluate the identification capability of the model (Table 3). Regarding the performance across different infection stages, the model's identification

precision was relatively limited during the initial stage when disease features were weak. However, by the fourth day post-inoculation, the discriminant accuracy (ACC_{day4}) improved to 85.94%, and further increased to 87.01% by the fifth day (ACC_{day5}), representing a significant enhancement in performance. According to phenotypic observations, natural symptoms of muskmelon powdery mildew typically manifest on the seventh day post-inoculation. This model can identify recessive infection features and complete disease prediction 2 to 3 days in advance, with early prediction accuracy consistently exceeding 85%. These results fully validate the feasibility and superiority of the PLS-DA model based on multispectral 3D point clouds for the early warning of muskmelon powdery mildew. This approach effectively overcomes the limitations of manual visual observation and provides precise technical support for the early detection and control of the disease.

Table 3. The average recognition accuracy of muskmelon powdery mildew from the *n*-th day post-inoculation onwards.

The *n*-th Day Post-Inoculation Onwards	Training Set Accuracy (%)	Validation Set Accuracy (%)	Average Accuracy (%)
1-th	83.49%	76.78%	80.14%
2-th	85.32%	80.18%	82.75%
3-th	86.58%	82.74%	84.66%
4-th	86.61%	85.27%	85.94%
5-th	87.29%	86.73%	87.01%
6-th	87.45%	88.69%	88.07%
7-th	88.42%	88.93%	88.68%
8-th	88.93%	89.73%	89.33%
9-th	89.59%	91.07%	90.33%
10-th	86.66%	93.75%	90.21%
11-th	86.36%	87.50%	86.93%

4. Discussion

4.1. Comparison with Similar Studies and Applicability of the Model

In previous studies, near-infrared spectroscopy was widely adopted for plant disease detection, and most analyses were performed using spectra collected from detached leaves or the average spectra of plant canopies. Zhao et al. combined VIS/NIR and NIR spectral data and employed a PCA-RBF model to diagnose tomato leaf mold, achieving 99.3% on the prediction set. High spectral imaging has achieved high accuracy in the detection of leaf diseases. However, this approach requires leaf sampling and laboratory measurement, which restricts its in situ application. Although certain achievements have been made in plant disease detection using canopy spectra, for instance, hyperspectral imaging was utilized to identify infections caused by *Fusarium commune* and *Rhizoctonia solani* in pakchoi plants, achieving a detection accuracy of 95.9% [16]. However, when near-infrared hyperspectral imaging is applied to collect canopy average spectra for plant disease detection, multiple drawbacks remain. Leaf occlusion, the influence of plant 3D structure on spectral reflectance calibration, as well as the requirement for samples with identical growth periods and similar canopy structures, all impair the generalizability of models. To solve these problems, three-dimensional multispectral point clouds have been developed by researchers for the detection of plant physiological and biochemical parameters. Roscher et al. integrated hyperspectral imaging with 3D point cloud reconstruction to build hyperspectral 3D plant models, which improved the detection accuracy of Cercospora leaf spot disease symptoms on sugar beet plants [24]. Xiao et al. employed multi-view spectral images combined with the Structure from Motion (SfM) algorithm, using only a single multispectral sensor to construct a 3D CLS (Cercospora leaf spot) point cloud model. The approach achieved a disease

severity classification accuracy of 75%, and the estimated disease incidence exhibited strong agreement with ground-truth measurements, yielding an RMSE of 8.4% [25]. Furthermore, after the construction of 3D spectral point clouds of plants, spectral reflectance must be calibrated according to their three-dimensional spatial structures prior to disease detection. Therefore, relevant explorations proposed a novel method for generating high-quality plant three-dimensional multispectral point clouds by fusing a snapshot spectral camera and an RGB-D depth camera, combined with an improved SURF-Demons registration algorithm and hemispherical reference body correction, significantly enhancing the spectral accuracy of 3D multispectral point clouds [29]. However, this method requires a dual-camera system (RGB-D and multispectral), which entails higher costs and increases data processing time and errors during the image registration step, thereby limiting its applicability in large-scale field deployment. This study can provide an early warning of natural symptom manifestation 2–3 days in advance. This method enables the early detection of powdery mildew in melon seedlings at any growth stage and exhibits favorable generalization performance.

All experiments in this study were conducted on a self-developed high-throughput 3D phenotyping platform for greenhouses, with customized data processing software developed in-house. The platform can automatically perform 3D multi-view image acquisition, 3D multispectral point cloud reconstruction, and reflectance calibration for plant samples. Its layout can be flexibly expanded according to the greenhouse space, achieving a maximum detection throughput of 1440 plants per day. In this study, multispectral canopy images were collected using fixed multi-view angles, which limits the adaptability of the method for large plants with dense and closed canopies. This represents a major limitation of our approach. To address this issue, future work will adopt dynamically adjustable multispectral camera positions to acquire comprehensive multi-angle plant images, eliminate detection blind areas in dense canopies, and further expand the applicability of the method. Furthermore, in the experiment, a fixed halogen lamp was adopted, and all measurements were conducted in a dark environment. The positions of the light source and multispectral camera remained stationary throughout the test. For practical application, any suitable light source system can be used, provided that the relative position between the multispectral camera and the light source is fixed. A 3D light field distribution model established with the hemispherical white reference can be used to calibrate the 3D multispectral reflectance of plants and detect their physiological and biochemical parameters. Overall, the proposed method is suitable for high-throughput disease detection of plants with relatively sparse canopies using greenhouse phenotyping platforms. Its direct field application is constrained by uncontrollable natural illumination and complex environmental interference. This limitation can be mitigated in future studies by equipping light-shielded chambers and standardizing data acquisition conditions to facilitate field deployment.

4.2. Advantages and Limitations of the Method

Advantages: The 3D multispectral point clouds of plants were reconstructed using a single multispectral camera in this study. The hemispherical white reference was innovatively combined with three-dimensional structural parameters to achieve accurate calibration of multispectral reflectance, which effectively improved the detection performance of melon powdery mildew. This technique supports in situ and non-destructive detection for whole plants. Since the training samples covered the entire infection cycle of powdery mildew on melon seedlings, the established model possessed strong robustness and generalization ability. Limitations: Firstly, the relative position between the light source and the camera of the data acquisition device must be kept fixed. Recalibration of the correction model is required once the operating condition of the equipment changes. Secondly, restricted by the field of view, this method is only applicable to seedlings rather

than mature plants with expanded canopies. Thirdly, the average spectrum of the whole plant was adopted as the input feature. The mixed errors caused by spectral heterogeneity inevitably led to a decrease in detection accuracy.

4.3. Future Research

In future research, deep learning algorithms together with characteristic band screening strategies will be adopted to further improve the accuracy of disease detection. Meanwhile, graded monitoring for powdery mildew with different infection severities will be carried out. Spectral features of lesion areas will be precisely extracted to optimize the recognition model and achieve higher detection accuracy. Furthermore, pixel-level visualization of disease detection results for whole plants will be realized to diversify the forms of disease analysis and result presentation.

5. Conclusions

Based on multi-view 3D reconstruction and multispectral imaging, this study proposed a multispectral data extraction method utilizing bidirectional projection between 2D images and 3D point clouds, achieving the efficient construction of 3D multispectral point clouds for both muskmelon plants and standard hemispherical white references. First, the YOLOv8 model was employed to achieve automated extraction of spatial hemispherical white reference targets, reaching an identification precision and recall of 97% and 99%, respectively. This provided a data foundation for background removal and 3D spatial characteristic parameter extraction of the hemispherical white reference 3D multispectral point clouds. Second, a spatial light field distribution model was constructed based on the 3D spatial characteristics of the hemispherical white reference. Research indicated that when the threshold for the angle between the projection vector and the normal vector was set to 20°, the model reached an optimal balance between sampling integrity and radiation accuracy. The coefficients of determination (R^2) for the training and validation sets were 0.885 and 0.872, respectively. This spatial light field distribution model significantly eliminated the spatial heterogeneity of radiance within the greenhouse, reducing the coefficient of variation (CV) of the point clouds at different spatial heights from an original maximum of 45.5% to within 2.4%, while stabilizing the relative reflectance above 95%. Finally, a PLS-DA discriminant model for muskmelon powdery mildew was constructed based on the calibrated mean reflectance of the 3D multispectral point clouds. The results showed that the average discriminant accuracy for muskmelon powdery mildew across the entire time series was 80.79%. The average accuracy of the model rose to over 85.94% starting from the fourth day post-inoculation, enabling early warning 2–3 days in advance of natural symptom manifestation. In summary, this research not only overcomes the limitations of traditional visual observation and 2D spectral scanning but also provides efficient and robust technical support for the intelligent perception, identification, and precision plant protection of facility horticultural crops.

Author Contributions: Conceptualization, Z.H., Q.G., H.C. and Y.H.; Data curation, Z.H.; Formal analysis, Z.H. and Q.G.; Funding acquisition, Y.H.; Investigation, Z.H. and Q.G.; Methodology, Q.G., L.F. and Y.H.; Project administration, Z.H.; Resources, L.F. and Z.H.; Software, Q.G. and Y.H.; Supervision, H.C.; Validation, Q.G.; Visualization, Z.H.; Writing—original draft, Z.H. and Q.G.; Writing—review and editing, Z.H., Q.G., L.F., H.C. and Y.H. All authors have read and agreed to the published version of the manuscript.

Funding: This research was funded by the National Natural Science Foundation of China, grant number 32572180.

Data Availability Statement: The data presented in this study are available on request from the corresponding author due to restrictions.

Conflicts of Interest: The authors declare no conflicts of interest.

References

1. Ercan, U.; Sonmez, I.; Kabas, A.; Kabas, O.; Zyambo, B.C.; Gölükcü, M.; Paraschiv, G. Quantitative Assessment of Brix in Grafted Melon Cultivars: A Machine Learning and Regression-Based Approach. *Foods* **2024**, *13*, 3858. [CrossRef] [PubMed]
2. Ivanova, Z.; Vasileva, K.; Velkov, N.; Grozeva, S. Evaluation of powdery mildew resistance in melon (*Cucumis melo* L.). *J. Agric. Sci. Technol.* **2019**, *10*, 279–284.
3. Cui, L.; Siskos, L.; Wang, C.; Schouten, H.J.; Visser, R.G.F.; Bai, Y.L. Breeding melon (*Cucumis melo*) with resistance to powdery mildew and downy mildew. *Hortic. Plant J.* **2022**, *8*, 545–561. [CrossRef]
4. Lenk, S.; Chaerle, L.; Pfündel, E.E.; Langsdorf, G.; Hagenbeek, D.; Lichtenthaler, H.K.; Van Der Straeten, D.; Buschmann, C. Multispectral fluorescence and reflectance imaging at the leaf level and its possible applications. *J. Exp. Bot.* **2007**, *58*, 807–814. [CrossRef] [PubMed]
5. Bai, D.; Shi, Q.; Wang, J.; Sun, F.; Li, H.; Lan, P. Early identification of melon powdery mildew based on hyperspectral feature extraction. *J. Chin. Agric. Mech.* **2024**, *45*, 172–177. [CrossRef]
6. Terentev, A.; Badenko, V.; Shaydayuk, E.; Emelyanov, D.; Eremenko, D.; Klabukov, D.; Fedotov, A.; Dolzhenko, V. Hyperspectral Remote Sensing for Early Detection of Wheat Leaf Rust Caused by *Puccinia triticina*. *Agriculture* **2023**, *13*, 1186. [CrossRef]
7. Zhang, X.M.; Vinatzer, B.A.; Li, S. Hyperspectral imaging analysis for early detection of tomato bacterial leaf spot disease. *Sci. Rep.* **2024**, *14*, 27666. [CrossRef] [PubMed]
8. Zhao, X.R.; Liu, Y.Y.; Huang, Z.B.; Li, G.A.; Zhang, Z.L.; He, X.H.; Du, H.L.; Wang, M.Q.; Li, Z.W. Early diagnosis of *Cladosporium fulvum* in greenhouse tomato plants based on visible/near-infrared (VIS/NIR) and near-infrared (NIR) data fusion. *Sci. Rep.* **2024**, *14*, 20176. [CrossRef] [PubMed]
9. Zhang, Y.Y.; Li, X.; Wang, M.Q.; Xu, T.; Huang, K.; Sun, Y.H.; Yuan, Q.C.; Lei, X.H.; Qi, Y.N.; Lv, X.L. Early detection and lesion visualization of pear leaf anthracnose based on multi-source feature fusion of hyperspectral imaging. *Front. Plant Sci.* **2024**, *15*, 1461855. [CrossRef] [PubMed]
10. Wu, G.S.; Fang, Y.L.; Jiang, Q.Y.; Cui, M.; Li, N.; Ou, Y.M.; Diao, Z.H.; Zhang, B.H. Early identification of strawberry leaves disease utilizing hyperspectral imaging combing with spectral features, multiple vegetation indices and textural features. *Comput. Electron. Agric.* **2023**, *204*, 107553. [CrossRef]
11. Ou, Y.M.; Yan, J.Y.; Liang, Z.Y.; Zhang, B.H. Hyperspectral Imaging Combined with Deep Learning for the Early Detection of Strawberry Leaf Gray Mold Disease. *Agronomy* **2024**, *14*, 2694. [CrossRef]
12. Liang, K.; Ren, Z.; Song, J.; Yuan, R.; Zhang, Q. Wheat FHB resistance assessment using hyperspectral feature band image fusion and deep learning. *Int. J. Agric. Biol. Eng.* **2024**, *17*, 240–249. [CrossRef]
13. Lay, L.; Lee, H.S.; Tayade, R.; Ghimire, A.; Chung, Y.S.; Yoon, Y.; Kim, Y. Evaluation of Soybean Wildfire Prediction via Hyperspectral Imaging. *Plants* **2023**, *12*, 901. [CrossRef] [PubMed]
14. Castro-Valdecantos, P.; Egea, G.; Borrero, C.; Pérez-Ruiz, M.; Avilés, M. Detection of fusarium wilt-induced physiological impairment in strawberry plants using hyperspectral imaging and machine learning. *Precis. Agric.* **2024**, *25*, 2958–2976. [CrossRef]
15. Niu, Z.Z.; Li, Y.K.; Moncada, J.D.S.; Johnson, W.; Lang, E.B.; Li, X.; Jin, J. Proximal hyperspectral imaging for early detection and disease development prediction of Septoria Leaf Blotch in wheat using spectral-temporal features. *Comput. Electron. Agric.* **2025**, *235*, 110400. [CrossRef]
16. Nguyen, D.H.D.; Tan, A.J.H.; Lee, R.; Lim, W.F.; Wong, J.Y.; Suhaimi, F. Monitoring of plant diseases caused by *Fusarium commune* and *Rhizoctonia solani* in bok choy using hyperspectral remote sensing and machine learning. *Pest Manag. Sci.* **2025**, *81*, 149–159. [CrossRef] [PubMed]
17. Bao, D.; Zhou, J.; Bhuiyan, S.A.; Adhikari, P.; Tuxworth, G.; Ford, R.; Gao, Y.S. Early detection of sugarcane smut and mosaic diseases via hyperspectral imaging and spectral-spatial attention deep neural networks. *J. Agric. Food Res.* **2024**, *18*, 101369. [CrossRef]
18. Tapia, R.; Lee, W.S.; Whitaker, V.M.; Lee, S. Multiple Methods for Predicting Strawberry Powdery Mildew Severity from Field Canopy Reflectance Data. *Phytofrontiers* **2025**, *5*, 283–289. [CrossRef]
19. Chang, J.Y.; Walsh, J.J.; Mangina, E.; Ruan, J.; Negrao, S. AI-driven 3D point cloud analysis in plant phenotyping: A Systematic Review. *Smart Agric. Technol.* **2026**, *13*, 101869. [CrossRef]
20. Li, Y.Z.; Liang, Z.; Liu, B.; Yin, L.J.; Wan, F.H.; Qian, W.Q.; Qiao, X. Applications of 3D Reconstruction Techniques in Crop Canopy Phenotyping: A Review. *Agronomy* **2025**, *15*, 2518. [CrossRef]

21. Xie, P.Y.; Ma, Z.H.; Du, R.M.; Yang, X.; Jiang, Y.; Cen, H.Y. An unmanned ground vehicle phenotyping-based method to generate three-dimensional multispectral point clouds for deciphering spatial heterogeneity in plant traits. *Mol. Plant* **2024**, *17*, 1624–1638. [CrossRef] [PubMed]
22. Harandi, N.; Vandenberghe, B.; Vankerschaver, J.; Depuydt, S.; Van Messem, A. How to make sense of 3D representations for plant phenotyping: A compendium of processing and analysis techniques. *Plant Methods* **2023**, *19*, 60. [CrossRef] [PubMed]
23. Liu, H.J.; Lee, S.H.; Chahl, J.S. Registration of multispectral 3D points for plant inspection. *Precis. Agric.* **2018**, *19*, 513–536. [CrossRef]
24. Roscher, R.; Behmann, J.; Mahlein, A.K.; Dupuis, J.; Kuhlmann, H.; Plümer, L. Detection of Disease Symptoms on Hyperspectral 3D Plant Models. In Proceedings of the 23rd ISPRS Congress, Prague, Czech Republic, 12–19 July 2016; pp. 89–96.
25. Xiao, S.F.; Chen, H.C.; Hou, Y.G.; Shao, K.; Bi, K.Y.; Wang, R.L.; Sui, Y.; Zhu, J.Y.; Guo, Y.; Li, B.G.; et al. Investigating the 3D distribution of Cercospora leaf spot disease in sugar beet through fusion methods. *Comput. Electron. Agric.* **2024**, *224*, 109107. [CrossRef]
26. Yang, D.N.; Yang, H.J.; Liu, D.F.; Wang, X.L. Research on automatic 3D reconstruction of plant phenotype based on Multi-View images. *Comput. Electron. Agric.* **2024**, *220*, 108866. [CrossRef]
27. Zhang, L.B.; Jin, J.; Wang, L.J.; Huang, P.K.; Ma, D.D. A 3D white referencing method for soybean leaves based on fusion of hyperspectral images and 3D point clouds. *Precis. Agric.* **2020**, *21*, 1173–1186. [CrossRef]
28. Zhang, L.; Jin, J.; Wang, L.; Rehman, T.U.U.; Gee, M.T.T., Jr. Elimination of Leaf Angle Impacts on Plant Reflectance Spectra Using Fusion of Hyperspectral Images and 3D Point Clouds. *Sensors* **2023**, *23*, 44. [CrossRef] [PubMed]
29. Xie, P.Y.; Du, R.M.; Ma, Z.H.; Cen, H.Y. Generating 3D Multispectral Point Clouds of Plants with Fusion of Snapshot Spectral and RGB-D Images. *Plant Phenomics* **2023**, *5*, 0040. [CrossRef] [PubMed]
30. MacDonald, M.T.; Esau, T.J.; Bilodeau, M.F. Exploring the potential of two vegetative indices, normalized difference vegetation index (NDVI) and enhanced vegetation index 2 (EVI2), to estimate balsam fir nutrition using uncrewed aerial vehicles and multispectral sensing. *Can. J. Plant Sci.* **2025**, *105*, 1–14. [CrossRef]
31. Bolya, D.; Zhou, C.; Xiao, F.; Lee, Y.J. YOLACT: Real-time Instance Segmentation. *IEEE Trans. Pattern Anal. Mach. Intell.* **2020**, *44*, 1108–1121.
32. Ul Haq, S.I.; Wang, G.B.; Khan, S.N.; Song, C.C.; Ma, C.; Zhang, X.J.; Lan, Y.B. Multi-dimensional optical remote sensing in agriculture: Spectral, angular, and spatial scaling for crop stress monitoring. *Smart Agric. Technol.* **2025**, *12*, 101583. [CrossRef]

Disclaimer/Publisher's Note: The statements, opinions and data contained in all publications are solely those of the individual author(s) and contributor(s) and not of MDPI and/or the editor(s). MDPI and/or the editor(s) disclaim responsibility for any injury to people or property resulting from any ideas, methods, instructions or products referred to in the content.